Chemical Engineering Journal 485 (2024) 149678

Contents lists available at ScienceDirect

Chemical Engineering Journal

journal homepage: www.elsevier.com/locate/cej

Magnetic resonance velocimetry of particle hydrodynamics in a three-dimensional draft tube spout-fluid bed

Jens P. Metzger [a,1], Boyuan Chen [a,b,1], Alexander Penn [d], Christian Guenthner [c], Klaas P. Pruessmann [c], Christoph R. Müller [a,*]

[a] Department of Mechanical and Process Engineering, ETH Zurich, 8092 Zurich, Switzerland
[b] Division of Chemistry and Chemical Engineering, California Institute of Technology, Pasadena, CA 91125, the United States of America
[c] Institute for Biomedical Engineering, ETH Zurich and University of Zurich, 8092 Zurich, Switzerland
[d] Institute of Process Imaging, Hamburg University of Technology, 21073 Hamburg, Germany

ARTICLE INFO

Keywords:
Draft Tube Spout-Fluid Bed
Magnetic Resonance Imaging
Granular Materials
Computational Fluid Dynamics and Discrete Element Method

ABSTRACT

Draft tube spout-fluid beds (DTSFB) are widely used in industry for processes that require intense mixing and high heat transfer between fluids and solid particles. The insertion of a draft tube compartmentalizes a slow-moving annular region from a high velocity flow in the draft tube, and thereby allowing for accurate control of the particle circulation rate and the gas contacting time. Due to these characteristics DTSFBs are a popular subject of experimental studies. However, the opaque nature of granular materials impedes the visual measurement of the solid flow inside DTSFB. The present study uses magnetic resonance imaging to measure non-invasively the hydrodynamics of the particulate phase in a three-dimensional DTSFB under various operational conditions at steady state. The obtained particle velocity maps provide with a previously unreported spatial resolution detailed insight into the flow dynamics of particles. From these maps, we characterize the particle entrainment from the annular region into the draft tube and we observe a vena contracta flow for low gap heights, as well as a linear dependence between the particle velocity in the draft tube and the spouting gas velocity. Moreover, the spouting gas flow can induce a suction effect that channels gas from the annulus to the draft tube and suppresses gas bubbling in the annular region. The experimental data is made available to serve as validation test cases for numerical simulations.

1. Introduction

Spout-fluid beds (SFBs) are an important class of reactors used in many industrial settings. SFBs are known to combine the advantages of a spouted and a fluidized bed by introducing a controlled region of fast fluid–solid flow to a fluidized bed, and by reducing the dead zones and increasing solid particle mixing in the annular region of a spouted bed [1–3]. As such, SFBs have been utilized in industrial applications in which superior heat and mass transfer between solids and fluids and stable solid circulation pattern are required, e.g., in particle drying [4], coating [5,6], combustion [7], gasification [8] and mixing [9].

The incorporation of a draft tube into a SFB results in a so-called draft tube spout-fluid bed (DTSFB). Studies have shown that DTSFBs require a lower spouting gas flow rate and a higher bed height for the spout to occur compared to a SFB, thereby increasing the energetic and material efficiencies of the operation [10–12]. Additionally, the insertion of a draft tube allows for a significantly more accurate control over the solid circulation rate and the gas contacting time [10,13–15], both of which are crucial to control better large scale units.

Previous studies have focused on the key global parameters that determine the effectiveness of DTSFBs. Empirical correlations have been given for the determination of the minimum spouting velocity [11], the solid circulation rate [10,13,14,16,17], the gas flow [10,18,19] and the pressure drop in the draft tube and the annulus [10,17,20,21].

However, the detailed hydrodynamics of DTSFBs are extremely difficult to study for two main reasons. First, there is a large variation in particle concentration and particle velocity between the annular region and the draft tube, often spanning up to two orders of magnitude. But

* Corresponding author at: Laboratory of Energy Science and Engineering, Department of Mechanical and Process Engineering, ETH Zurich, 8092 Zurich, Switzerland.
E-mail address: muelchri@ethz.ch (C.R. Müller).
[1] Shared first authors.

https://doi.org/10.1016/j.cej.2024.149678
Received 20 October 2023; Received in revised form 17 January 2024; Accepted 13 February 2024
Available online 17 February 2024

more importantly, due the opaque nature of granular materials, the internal processes of a full three-dimensional DTSFB are not accessible by visual techniques from the outside. Instead, DTSFBs have been studied by means of pseudo-2D beds [22,23] or semi-circular columns [10,13,14,18,19,24–26], yet with the consequence, that wall effects will influence the particle packing and the particle velocity fields close to the wall [25,27–30]. Alternatively, optical probes [28,29,31,32] can be inserted locally into the bed probing the particle flow yet being intrusive to the process.

Tomographic techniques using X-rays [33,34,35], positron emission [33,36–39], magnetic tracers [40,41], electrical capacitance [42], and magnetic resonance [43–46] have been proven very useful for the non-invasive study of spouted and spout-fluid beds. However, to the best of the authors' knowledge, few tomographic studies have been performed on a DTSFB quantifying the hydrodynamics of the particle phase. Yet, this insight into the process is crucial for the identification of dead zones.

On the other hand, numerical simulations are widely used to study spouted beds with [22,47–51] and without [32,52–54] draft tubes. However, these systems contain a complex multiphase flow with large gradients in fluid velocity and void fraction and are thus often used as validation test cases for force models, e.g., drag models. To this end, high-quality experimental data are needed as validation reference to ensure accurateness of the simulations [38,42,55].

In this study, magnetic resonance imaging (MRI) was utilized to non-invasively measure time-averaged particle velocity and voidage data in steady-state, full three-dimensional DTSFBs as a function of draft tube positions, background fluidization gas flow and spouting gas flow. Specifically, qualitative solid distribution maps and quantitative particle velocity maps in a DTSFB were obtained. The maps resolve in detail the prevailing particle flow features including a previously unobserved vena contracta at the draft tube inlet when operated at low gap height. Additionally, a linear scaling of the particle velocity profile in the draft tube as a function of the spouting gas flow is derived. Also, increasing the spouting gas flow and lowering the gap height of the draft tube suppresses the formation of gas bubbles in the annular region, which was further supplemented by a computational fluid dynamics and discrete element method (CFD-DEM) simulation that investigates the gas flow and pressure gradient in the DTSFB. The particle velocity maps acquired for various operation conditions are made available [56] to help the validation and advancement of the numerical modelling of two-phase granular systems.

2. Materials and method

The cylindrical lab-scale DTSFB used in this work has an inner diameter of $D_b = 190$ mm and a height of $H = 277$ mm. A $L = 150$ mm long draft tube with an inner diameter of $D_i = 30$ mm was mounted in the center of the system such that the gap height H_g was adjustable from 5 mm to 20 mm (measured from the bottom of the bed). Two separate lines of pressurized air were used to introduce a background fluidization gas flow into the entire system and an additional spouting gas flow via an orifice with a diameter of $D_o = 8$ mm at the center of the bottom plate. The flow in each gas line was controlled with a separate mass flow controller (Bronkhorst Mass Stream D-6383-DR/BJ2.8 for the background fluidization gas flow and F-203AV for the spouting flow). The background fluidization gas flow was homogeneously distributed into the bed through a 10 mm thick acrylic distributor plate with evenly spaced holes of 0.5 mm in diameter arranged in a hexagonal pattern with a 2.25 mm spacing between the individual holes, see Fig. 1. The hole pattern covers the entire distributor plate except for a circular area of 13 mm in diameter, in which the orifice for the spouting gas flow is placed. For the values of the background fluidization gas flow used here, the pressure drop across the distributor ranges between 300 and 390 Pa (measured using a KAL 84, Halstrup-Walcher GmbH). The temperature and humidity of the background fluidization gas ~ 20 °C and 15 % r.h., respectively (measured using a GFTB 200, GMH Messtechnik GmbH). The humidity was kept low to avoid swelling of the particles used in the DTSFB. The background fluidization velocity U_{bg} was varied between 1 and 1.2 times the minimum fluidization velocity U_{mf} of the particles used, whereas the spouting gas velocity U_S was varied between 50 and 250 × U_{mf} to achieve a dispersed spouting behavior. Here, U_S refers to the discharge velocity of the spouting gas flow directly at the orifice of the diameter D_0. The pressure drop across the orifice ranges between 1.5 and 27.2 kPa. The ranges of flow rates were chosen such that a stable particle circulation at the lowest U_{bg} and U_S settings was guaranteed, i.e., a circulation pattern in which the particles enter the draft tube from the annular region via the gap between the draft tube and the bottom of the bed and are subsequently spouted out of the draft tube to replenish the particles in the annular region. The top of the DTSFB is covered with a thin, fine mesh that is penetrable for gas flow and retains particles inside the fluidized bed. For $U_S/ U_{mf} > 50$, particles spouting out of the draft tube can hit the mesh and fall back to the annular region, i.e., the mesh affects the trajectories of the particles in the particle-lean head space of the DTSFB. However, the mesh has only marginal effect on the hydrodynamics in the annular region and the dynamics inside the draft tube. A steady-state operation was usually achieved within a few seconds. Hence, all the measurements were acquired at steady state conditions.

Tailored spherical particles as described in Ref. [57] were used owing to their favorable mechanical and magnetic resonance properties. The particles consist of a middle-chain triglyceride oil core that takes up 73 wt% of the total particle mass encapsulated by a 100-µm-thick agar shell. The resulting particles have a diameter of $d_p = 1.02 \pm 0.12$ mm, density $\rho_p = 1040$ kg m^{-3}, dynamic angle of repose $\Theta_r = 28 \pm 2°$,

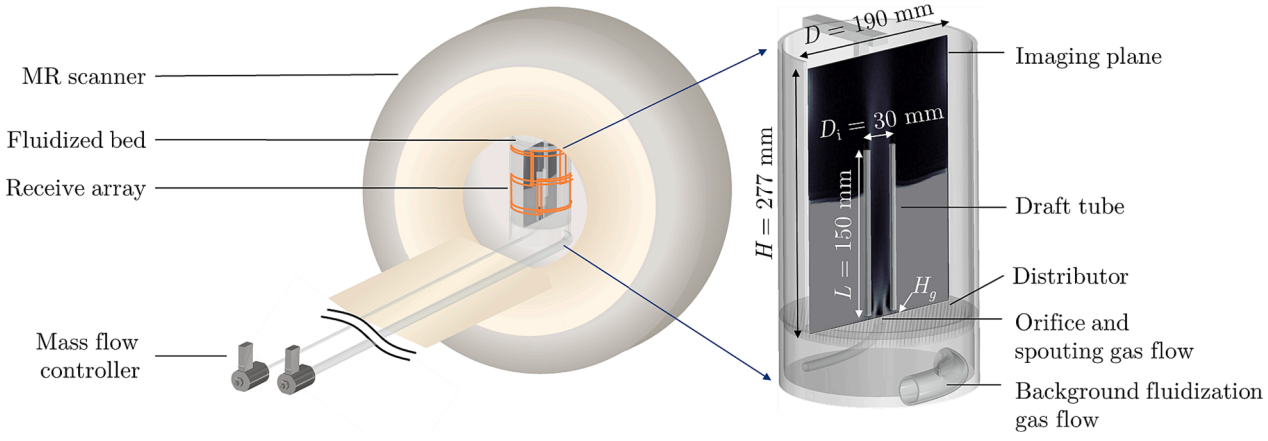

FIG.1. Experimental setup of the draft tube spout-fluid bed (DTSFB) and its placing in the magnetic resonance scanner.

friction coefficient $\mu = 0.54 \pm 0.05$, and a coefficient of restitution $e = 0.70 \pm 0.03$ [57]. The particles were designed to have a relatively large T_2 of 1.75 ms in a 3-T magnetic resonance imaging (MRI) system and a high spin density to increase the signal-to-noise ratio (SNR) for better imaging. The measured minimum fluidization velocity of the particles is $U_{mf} = 0.25$ m/s and hence fall in between Group B and D of Geldart's classification [57,58].

Before each set of measurement, the DTSFB was fully packed with particles to establish a baseline that is used to correct for background phase offsets as well as non-uniform coil sensitivity. Subsequently, the experiments were performed on a bed filled with particles to a height of $H_b = 100$ mm before the insertion of the draft tube, such that a constant amount of particles was used in each experiment (ca. 1.75 kg). The pressure drop across the bed at minimum fluidization is 600 Pa, i.e., twice the pressure drop of the distributor.

For the imaging of the system, a medical-grade human MRI device was used (Achieva 3.0 T, Philips Healthcare). The bed was placed into a custom-built 16-channel radio frequency (RF) receive coil as reported in Ref. [57]. Turbo field echo (TFE) sequences were applied with 40–80 signal averaging steps and a repetition time (TR) of 11 ms to acquire the signal intensity and phase-contrast velocimetry data of the particles in the DTSFB. The employed TFE sequence has a flip angle of 15°, an echo time of 2.93 ms and performs phase and frequency encoding in the horizontal and vertical direction, respectively. The use of TFE allowed for a user defined waiting time during which spins could recover prior to a subsequent RF excitation allowing for a high signal-to-noise ratio.

For all settings of the DTSFB studied, four scans of the central, vertical slice of the DTSFB were acquired with 2 mm × 2 mm in-plane spatial resolution and 10 mm slice thickness. Due to the high spatial variation of particle velocity in this vertical slice with low particle velocities in the annular region (ca. 5 cm/s) and high velocities in the draft tube (ca. 300 cm/s), four different phase-encoding velocities (VENC) were required to resolve adequately the velocity components in the vertical and horizontal directions in the annular and in the draft tube regions. The applied VENC values were in the range between 7.5 cm/s and 500 cm/s and were adapted based on the expected prevailing maximum velocity in the respective region.

The acquired phase-contrast images first underwent a phase-unwrapping procedure to correct for velocity aliasing in the high-velocity regions. The four images with high and low VENCs can be combined to create a high-resolution velocity map for the entire system, as shown in Fig. 2. For a limited number of DTSFB settings, additional horizontal slices (2 mm × 2 mm spatial resolution and 10 mm thickness) were acquired to probe the distribution of particle velocities in the cross-section of the bed.

In addition to the experimental measurements, numerical simulations using the discrete element method combined with computational fluid dynamics (CFD-DEM) were performed to investigate the gas flow pattern in the annular region of the DTSFB. To this end, a three-dimensional model of the DTSFB resembling the experimental setup was modelled in cfdemCoupling [55]. A k-ω-SST turbulence model [59] was chosen to account for the turbulent nature of the gas flow in the draft tube. The Koch-Hill-model [60] was used to model the drag force between the gas and particle phase. The simulations were run until steady-state conditions were established. The resulting gas and particle fields were time averaged for 3 s. A detailed list of the simulation settings can be found in the Supplementary Material S1.

3. Results and discussions

3.1. Flow visualization from MRI velocimetry measurements

MRI data from four separate velocity measurements (owing to the large velocity gradient in the DTSFB) were acquired and used to reconstruct a single particle flow map in the vertical plane. Each MRI scan yields two data sets: a signal intensity map and a phase-contrast velocity map.

Fig. 2 (a) showcases the signal intensity data for the setting: $U_{bg}/U_{mf} = 1$, $U_S/U_{mf} = 250$, and $H_g = 5$ mm. The signal intensity data is taken from the scan with the highest VENC settings (500 cm/s) as it suffers only negligibly from dephasing due to the VENC gradients [61]. The intensity map is normalized by the signal intensity map of a stationary bed fully packed with particles. The normalization of the signal intensity data with the packed bed data reduces coil sensitivity artifacts and B_1 heterogeneities allowing to provide a qualitative representation of the time-averaged particle concentration inside a steady-state DTSFB. The lighter regions in the image correspond to a higher particle concentration and the darker regions correspond to lower concentrations. From Fig. 2 (a), a draft tube region with low signal intensity and an annular region surrounding the draft tube with a high signal intensity are immediately discernable. The segmentation of the velocity maps is based on this distinction. For example, the velocity measurement that

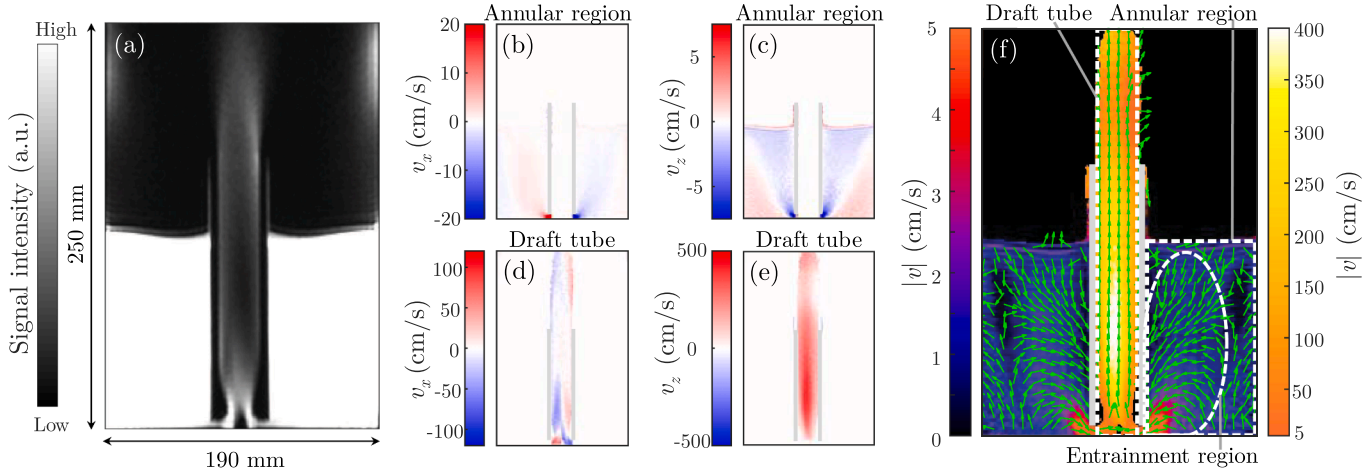

FIG.2. Visualization of the signal intensity and particle velocity profile using magnetic resonance imaging for a DTSFB operating at $U_{bg}/U_{mf} = 1$ $U_S/U_{mf} = 250$, and $H_g = 5$ mm. (a) Normalized signal intensity map. The brightness of the image correlates with the particle concentration. (b-e) Particle velocity maps encoding the horizontal velocity v_x (b, c) and vertical velocity v_z (d, e) cropped in accordance with (a) to only show the annular region of the bed (b, c) or the draft tube (d, e), respectively. (f) Composite velocity map combining the maps from (b-e). The background color shows the magnitude of the particle velocity (left colorbar for the annular region, right colorbar for the draft tube region), and the arrows indicate the flow direction (arrow length is at unit scale). All data is acquired from a 10 mm thick vertical slice through the center of the DTSFB and averaged over 40 – 80 acquisitions, i.e., 55 – 110 s acquisition time.

encodes the horizontal velocity with a maximum velocity of 40 cm/s captures the horizontal velocity in the annular region only, hence only the data that overlaps with the annular regions in Fig. 2 (a) is kept in Fig. 2 (b). The segmented velocity components in the draft tube and the annular regions (Fig. 2 (b-e)) are subsequently combined to produce a composite velocity map as shown in Fig. 2 (f).

It is worth noting that the signal intensity of a TFE sequence is prone to attenuation due to flow artifacts and T_2*-decay impeding a quantitative measurement of particle concentration. Specialized MRI sequences [62,63] are required to counteract these artifacts; however, such sequences are very time-consuming (in the order of one hour per scan) and not performable on the hardware used in this study. In the following, particle concentration measurements are regarded as qualitative. Nevertheless, the velocity measurements are not subject to the aforementioned artifacts and are thus quantitative.

As seen in Fig. 2 (f), the draft tube region is characterized by a low particle concentration and a dominant upward particle motion with a high velocity approaching 500 cm/s (Fig. 2 (e)), whereas the annular region is characterized by a much higher particle concentration and a dominant horizontal particle motion approaching only 20 cm/s (Fig. 2 (b)). Additionally, the highest particle velocity observed in the system is along the centerline of the draft tube, i.e., the region in which the particle concentration is lowest. The vector plot in Fig. 2 (f) shows an entrainment region from where particles in the annular region are drawn into the draft tube through the gap between the bottom of the bed and the draft tube. The particle velocities increase when approaching this gap. A zone of low particle velocity can be found in the bottom corners of the annular region, indicating dead zones from where particles are not drawn towards the draft tube and thus do not participate in the overall particle circulation pattern. Although, the velocity map in Fig. 2 (f) gives the impression that the horizontal velocities of the particles in the dead zone point away from the draft tube, this behavior is an artifact caused in the phase-encoding step of the velocity measurement. Due to the very small actual velocity of the particles in the dead zone, the measured phase of the signal becomes very susceptible to magnetic field imperfections such as B_0 inhomogeneities, gradient nonlinearities, and abrupt changes in the magnetic susceptibility of material at the outer edge of the annular region. This leads to spurious velocity assignments. Regions closer to the center of the bed and regions with higher particle velocity are less affected by these artifacts.

The effective solid flow pattern in a DTSFB depends on the operational conditions, viz. H_g, U_{bg}/U_{mf}, and U_s/U_{mf}. Fig. 3 illustrates both the commonality and variability in the particle flow by showing the signal intensity maps and the velocity maps for nine different operational settings. While the general observations made in Fig. 2 hold in all measured cases, variations in the spout are noticeable. We observe that when increasing H_g, more particles enter the draft tube leading to an increase in signal intensity. However, the overall particle velocity in the draft tube does not change appreciably with varying H_g at constant U_s/U_{mf} (Fig. 3 (a-f)). As expected, the particle velocity in the draft tube increases with increasing spouting gas flow. This is because the particles gain more upward momentum, flow faster and disperse inside the draft tube, simultaneously leading to a lower particle concentration inside the draft tube. This effect becomes obvious when comparing the first and

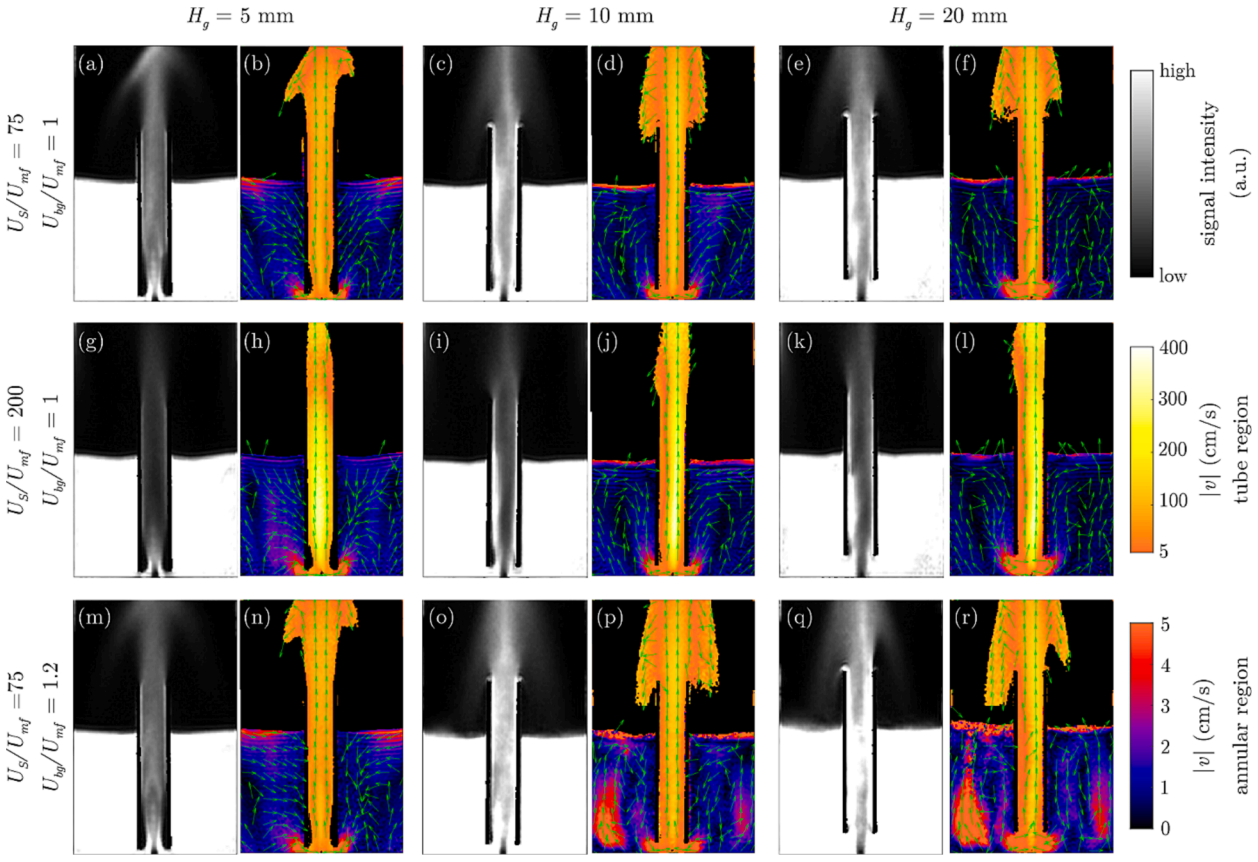

FIG.3. Signal intensity map (left, grey scale) and particle velocity map (right, color) for three gap sizes $H_g = 5$ mm (first column), 10 mm (second column), and 20 mm (third column). The first row shows cases with low spouting gas flow ($U_S/U_{mf} = 75$) and incipient background fluidization ($U_{bg}/U_{mf} = 1$). In the second row, the spouting gas flow is increased ($U_S/U_{mf} = 200$) at constant U_{bg}, whereas the third row shows an increased background fluidization ($U_{bg}/U_{mf} = 1.2$) at constant U_S. All data are acquired in a 10 mm vertical slice through the center of the DTSFB. (a, b) $U_S/U_{mf} = 75$, $U_{bg}/U_{mf} = 1$, $H_g = 5$ mm. (c, d) $U_S/U_{mf} = 75$, $U_{bg}/U_{mf} = 1$, $H_g = 10$ mm. (e, f) $U_S/U_{mf} = 75$, $U_{bg}/U_{mf} = 1$, $H_g = 20$ mm. (g, h) $U_S/U_{mf} = 200$, $U_{bg}/U_{mf} = 1$, $H_g = 5$ mm. (i, j) $U_S/U_{mf} = 200$, $U_{bg}/U_{mf} = 1$, $H_g = 10$ mm. (k, l) $U_S/U_{mf} = 200$, $U_{bg}/U_{mf} = 1$, $H_g = 20$ mm. (m, n) $U_S/U_{mf} = 75$, $U_{bg}/U_{mf} = 1.2$, $H_g = 5$ mm. (o, p) $U_S/U_{mf} = 75$, $U_{bg}/U_{mf} = 1.2$, $H_g = 10$ mm. (q, r) $U_S/U_{mf} = 75$, $U_{bg}/U_{mf} = 1.2$, $H_g = 20$ mm.

second row of Fig. 3. The reduction of the signal intensity in the draft tube is more pronounced for $H_g = 5$ mm than for $H_g = 10$ mm and 20 mm (Fig. 3 (g, i, k)) indicating that the particle concentration in the tube becomes transport-limited at low H_g. When U_{bg}/U_{mf} is increased from 1 to 1.2, the signal intensity in the draft tube increases (i.e., a denser particle flow) for $H_g = 10$ mm (Fig. 3 (o)) and 20 mm (Fig. 3 (q)), but not significantly for 5 mm (Fig. 3 (m)), providing further evidence for a transport limitation for $H_g < 10 \times d_p$. This finding aligns with the design guidelines for draft tubes by Epstein and Grace [64].

Additionally, the following three observations were made for the particle distribution in the DTSFB studied here. First, most particles inside the draft tube accumulate near the wall of the draft tube. This agrees with the observations of Zhang et al. [65] and Zhang et al. [66] for riser tubes in fluidized beds. However, Saadevandi and Turton [25] found a particle-rich core in draft tubes at vertical positions $z \geq 30$ mm. This discrepancy can be explained by differences in the design of the gas inlet in the spout region. While Saadevandi and Turton [25] used a wide draft tube of diameter 104 mm and fluidized the entire draft tube via a sintered distributor plate, the present study uses a relatively small draft tube of 30 mm diameter. More importantly, the spouting gas is injected via an even smaller orifice (8 mm in diameter) creating an expanding spouting gas profile inside the draft tube that pushes particles towards the draft tube walls. The accumulation of particles near the wall of a small-diameter draft tube was also confirmed via numerical simulations (discussed further below).

Secondly, Fig. 2 (a) and Fig. 3 (a, g, m) reveal a vena contracta-like inflow structure at the bottom of the draft tube, whereby particles concentrate close to the centerline of the draft tube while voids are present close to the inner walls of the draft tube. This is because inertial particles are drawn through a small gap between the bottom plate and the draft tube with a high horizontal velocity and are subsequently redirected in the vertical direction due to the drag force imposed by the spouting gas flow. As shown in panels (g), (i), and (k) of Fig. 3, this vena contracta effect is clearly visible for $H_g = 5$ mm, but less pronounced in large values of H_g, i.e., for $H_g = 10$ mm to 20 mm.

The third observation is an asymmetry of the particle velocity in the annular region potentially caused by a slight maldistribution of the background fluidization gas flow through the distributor plate. When $U_{bg}/U_{mf} = 1.2$ (Fig. 3 (o-r)), gas bubbling occurs in the annular region for $H_g = 10$ mm and 20 mm, which will be described in Section 3.3. However, the degree of gas bubbling on the left side of the imaging plane is higher than on the right side, as indicated by a higher upward particle velocity on the left side of Fig. 3 (p) and (r). Furthermore, the distribution of solids in the draft tube is not axis-symmetric if the draft tube is positioned with $H_g = 10$ mm or 20 mm (Fig. 3 (c, e, i, k, o, q)). Here, particles with the highest velocity and lowest particle concentration are observed on the right-hand side of the centerline of the draft tube, an effect that will be discussed in more detail in the next section.

3.2. Velocity scaling in the draft tube

Following the discussion of the general flow structures observed in the DTSFBs, the motion of the particles inside the draft tube is further quantified. To this end, the particle velocity profiles at various positions inside the draft tube were extracted from the velocimetry data. For convenience, the vertical velocities of the particles are plotted as a

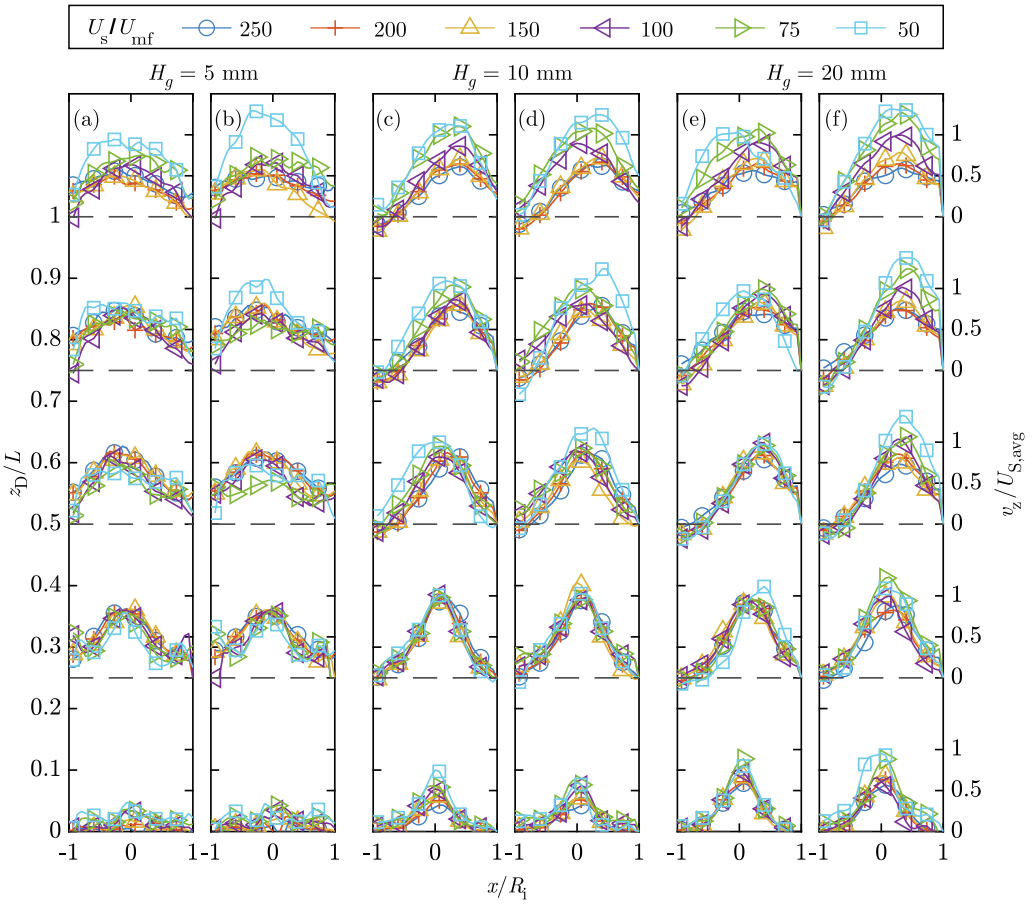

FIG.4. Radial profiles of the vertical particle velocity v_z normalized by the average superficial gas velocity in the draft tube $U_{S,avg}$, for three values of H_g and two values of U_{bg}/U_{mf}. All data are obtained in a 10 mm thick vertical slice though the center of the draft tube. z_D is measured from the bottom of the draft tube, i.e., $z_D = z - H_g$. (a) $H_g = 5$ mm, $U_{bg}/U_{mf} = 1$, (b) $H_g = 5$ mm, $U_{bg}/U_{mf} = 1.2$, (c) $H_g = 10$ mm, $U_{bg}/U_{mf} = 1$, (d) $H_g = 10$ mm, $U_{bg}/U_{mf} = 1.2$, (e) $H_g = 20$ mm, $U_{bg}/U_{mf} = 1$, (f) $H_g = 20$ mm, $U_{bg}/U_{mf} = 1.2$.

function of their dimensionless radial positions x/R_i at various dimensionless heights z_D/L (Fig. 4). Here, z_D refers to the axial position inside the draft tube with $z_D = 0$ being the bottom of draft tube and corresponding to $z = H_g$. The particle velocity profiles are expected to scale with the gas velocity inside the draft tube. Thus, the vertical particle velocity v_z is normalized by the average superficial gas velocity $U_{S,avg}$ inside the draft tube for each spouting condition. Here, the gas flow inside the draft tube is assumed to be incompressible (Ma < 0.15) and to comprise only the injected spouting gas flow, i.e., $U_{S,avg} = U_s\,(D_i/D_0)^2$.

When the vertical component of the velocity of the particles is normalized against $U_{S,avg}$, uniform particle velocity profiles are obtained for various values of U_S and U_{bg} and for a given H_g and axial position z/L in the draft tube. This observation confirms that the velocity profiles are self-similar and that there is a linear scaling of the particle velocity with $U_{S,avg}$ in the draft tube. The uniformity of the profiles is particularly well established at lower positions inside the draft tube (i.e., $z/L \leq 0.75$), whereas a higher variation among the profiles is observed at the upper end of the tube and for low spouting gas flows ($U_S/U_{mf} = 50$ and 75). This finding confirms that the profiles are self-similar in regions where the formation of the two-phase flow is dominated by the spouting gas flow. Moreover, the velocity profiles obtained for $U_S/U_{mf} \leq 75$ slightly deviate from the velocity profiles for $U_S/U_{mf} > 75$. This could indicate a change in the flow regime of the particles inside the draft tube for $U_S/U_{mf} \sim 75$ [17,21,23] or that there is a crossflow of gas from the annular region into the draft tube [10,14,18,19] violating the assumption that the gas flow in the draft tube exclusively comprises the injected spouting gas. The later effect will be discussed in Section 3.3.

Further, all cases depicted in Fig. 4 show a clear change in the shape of the velocity profile along the axial direction. For $H_g = 5$ mm, the vertical velocity is close to zero at $z_D/L = 0$, as the particles have just entered the draft tube horizontally, resulting in a low v_z. However, when increasing z_D/L to 0.25, the velocity profile becomes bell-shaped with the maximum velocity close to the centerline of the draft tube. This profile broadens and flattens with increasing values of z_D Close to the top of the tube, the velocity profiles almost resemble the exponential shape found in riser tubes of circulating fluidized beds [66]. This change in velocity profile is related to the fact, that the radial solid distribution changes with z_D/L (Fig. 3). When entering the draft tube, the particles are horizontally drawn to the center of the draft tube forming a dense spout around the injected spouting gas flow. This spout subsequently rises and spreads radially in the draft tube, pushing particles towards the wall of the draft tube for $z_D/L \geq 0.25$. Hence, the spout forms a lean fast moving core and a particle-rich, but slower moving ring close to the inner walls of the draft tube [65]. Although Saadevandi and Turton [25] found the distribution of solids to be dense in the center and lean at the walls of the draft tube, their particle velocity profile still agrees with the results obtained here.

For larger values of H_g, i.e., $H_g = 10$ mm or 20 mm (Fig. 4 (c-f)), the particle velocity profile in the draft tube becomes less radial symmetric compared to the profile obtained for $H_g = 5$ mm. Instead, the velocity profile resembles a skewed bell-shape in the upper half of the draft tube. This is because larger values of H_g lead to higher degree of particle entrainment in the draft tube, resulting in a less homogenous flow and aggregative spouting. Any small imperfection in the setup will lead to a preferential accumulation of particles on one side of the draft tube. The effect of particle enrichment at the walls of the draft tube is more pronounced for particles with a low coefficient of restitution [23] as for the agar particles used here.

Regarding the influence of U_{bg}/U_{mf} on the shape of the velocity profiles in the draft tube, there is no appreciable difference between the velocity profiles obtained for $U_{bg}/U_{mf} = 1$ and 1.2 at a given height z_D/L and H_g, i.e., comparing panels (a) and (b), (c) and (d), and (e) and (f), respectively. Hence, for sufficiently high values of U_S/U_{mf}, the spouting gas flow is the key parameter affecting the particle velocity in the draft tube.

3.3. Gas bubbling in the annular region

After examining the particle flow in the draft tube, we explored the motion of the particles in the annular region of the DTSFB. Here, Fig. 5 shows the lower section of the annular region for six experiments in which H_g and U_{bg}/U_{mf} were varied (an average of the left and right sides of the MRI acquired velocimetry data is shown).

Comparing the panels (a-c) in the first row of Fig. 5 (annular region is incipiently fluidized, i.e., $U_{bg}/U_{mf} = 1$), similar particle flow fields are obtained for varying values of H_g. Specifically, there is a region of high particle velocity close to the entrance of the draft tube where particles are entrained into the spout. This entrainment zone expands radially in the annular region of the DTSFB, whereby the magnitude of the particle velocity decreases rapidly both with increasing radial (x/R) and axial (z/H_b) position. For $H_g = 5$ mm, this entrainment zone penetrates far into the annular region ($x/R = 0.75$), whereas for $H_g = 10$ and 20 mm, the entrainment zone only reaches roughly up to $x/R = 0.4$ for $z < 0.1H_b$ into the annular region. Complementary to the entrainment zone, the annular region exhibits a distinct region at the bottom corner ($x/R = 1$, $z/H_b = 0$), where the particles do not move towards the draft tube and show indeed only very little motion. In this region the particles form a flowing zone that is separated from the entrainment zone. Hence, particles will have a very different residence time in the annular region depending on their radial position. This separated zone increases in size with increasing H_g.

The differences in the characteristics of the entrainment zone for varying H_g might be attributed to the following two reasons. First, a large H_g facilitates the motion of particles into the draft tube resulting in lower shearing forces that penetrate less deep into the annular region. Secondly, the spouting gas flow in the draft tube can work as a venturi nozzle, the suction of which increases with decreasing H_g. Due to the high gas velocity in the draft tube and the low particle concentration in the draft tube compared to the annular region, the draft tube acts as a pressure sink actively sucking in gas and particles from the annular region [18].

The leakage of gas from the annular region into the draft tube becomes clearer in the second row of Fig. 5 ($U_{bg}/U_{mf} = 1.2$). For $H_g = 10$ mm (e) and 20 mm (f), strong gas bubbling is observed in the annular region, which is expected for Geldart D particles at $U_{bg} \geq U_{mf}$. In velocity maps, gas bubbling is observed as an area of increased upward particle velocity. Fig. 5 (e) and (f) show that gas bubbling occurs near the outer wall of the DTSFB but not close to the draft tube. This is in accordance with visual observations during the experiments. The direction of particle motion in the annular region suggests a convection pattern, where particles in the bottom corner of the bed are transported upwards due to gas bubbling, and particles close to the draft tube move downwards into the entrainment region. Further, gas bubbling eliminates the dead zone observed for $U_{bg}/U_{mf} = 1$.

However, the size and the intensity of the gas bubbling region in the annular region decreases with decreasing H_g for a given U_S/U_{mf}. Fig. 5 (d) demonstrates that no gas bubbling occurs for $H_g = 5$ mm and $U_S/U_{mf} = 150$, although, U_{bg}/U_{mf} would be high enough to cause gas bubbling. This leads to the conclusion that gas from the annular region is drawn into the draft tube and bypasses the fluidized bed, such that the formation of gas bubbles in the annular region is suppressed.

A CFD-DEM simulation of the experimental settings shown in Fig. 5 (d) has been performed to prove the hypothesis that bubble suppression in the annular region is due to the suction effect of the spouting gas flow in the draft tube. The results of the simulation are shown in Fig. 6. The numerically obtained particle velocity map agrees well with the experimental data also showing the vena contracta in the draft tube. Further, the simulations indicate indeed that there is a net gas flow from the annular region into the draft tube reducing the superficial gas flow in the annular region (Fig. 6 (b)). The reason for this channeling is the pressure gradient between the annular region and the draft tube (Fig. 6 (c)), confirming gas leakage from the annular region into the draft tube. The

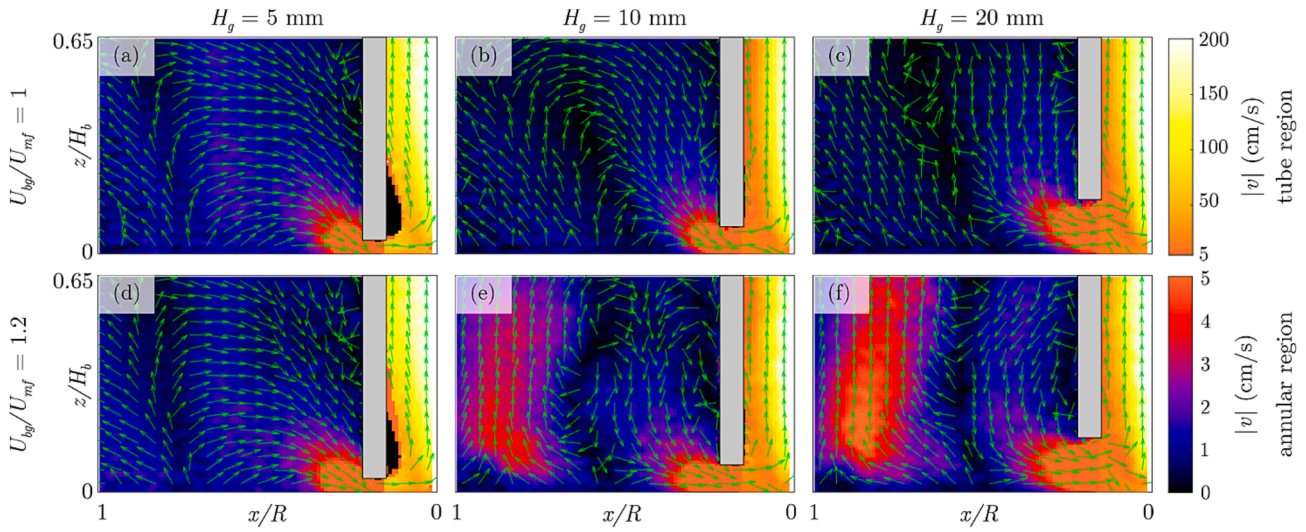

FIG.5. Particle velocity map in the annular region for three values of H_g = [5 mm, 10 mm, 20 mm] at U_{bg}/U_{mf} = 1 (top row) and 1.2 (bottom row). All data are acquired at U_S/U_{mf} = 150 and the left and the right side of the annular region are averaged. The wall of the draft tube is shown in grey. (a) U_{bg}/U_{mf} = 1.0, H_g = 5 mm. (b) U_{bg}/U_{mf} = 1.0, H_g = 10 mm. (c) U_{bg}/U_{mf} = 1.0, H_g = 20 mm. (d) U_{bg}/U_{mf} = 1.2, H_g = 5 mm. (e) U_{bg}/U_{mf} = 1.2, H_g = 10 mm. (f) U_{bg}/U_{mf} = 1.2, H_g = 20 mm.

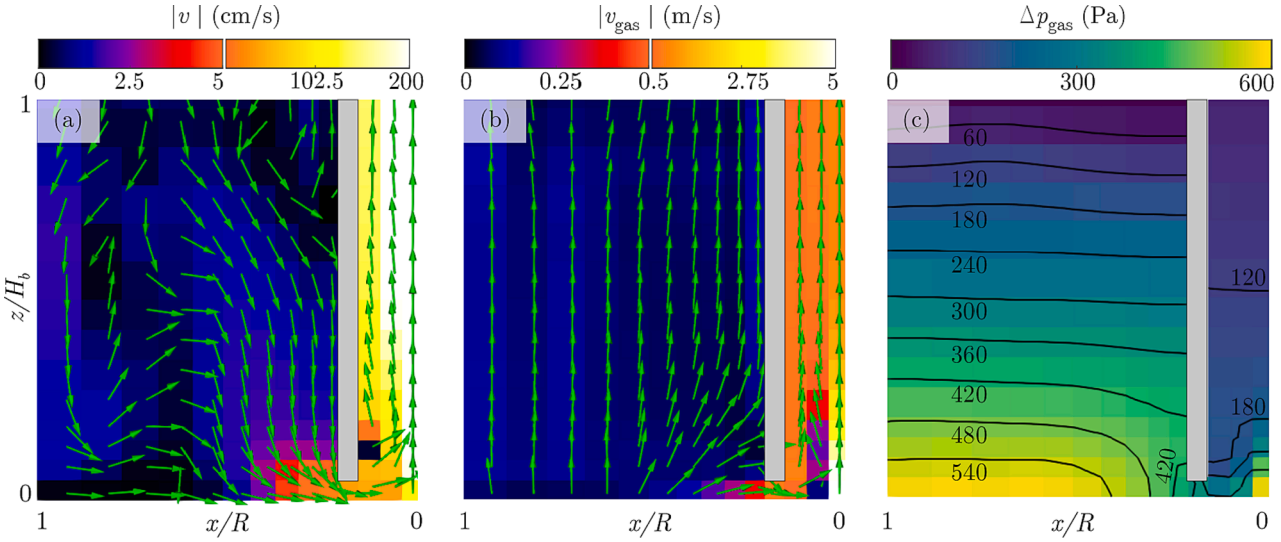

FIG.6. Results of a CFD-DEM simulation with H_g = 5 mm, U_{bg}/U_{mf} = 1.2, and U_S/U_{mf} = 150. The panels show the particle velocity map (a) and the gas velocity map (b), respectively. The background color depicts the velocity magnitude and the arrows (unit scale) show the flow direction. (c) Gas pressure map with isobars (black lines). All data are obtained from the left half of a vertical plane through the center of the DTSFB and are time averaged over 3 s. The grey insert shows the wall of the draft tube.

pressure gradient is a result of the "venturi"-like effect caused by the high spouting velocities in the draft tube. In addition to gas leaking from the annular region into the draft tube via the gap under the draft tube, it is possible that the low gas pressure in the draft tube favors the background fluidization gas to preferentially flow through orifices of the distributor that are located inside the draft tube area. This effect might occur due to the relatively low pressure drop of the distributor compared to the fluidization pressure drop of the bed and might further deplete the fluidization gas flow in the annular region. However, this effect is not observable in the simulations, as the distributor is modelled as a uniform inlet velocity.

The degree of gas leakage from the annular region depends on U_S as confirmed in Fig. 7 which compares two setting of U_S/U_{mf} for a DTSFB with H_g = 10 mm and U_{bg}/U_{mf} = 1.2. With increasing U_S, the size of the bubbling region is reduced and migrates towards the outer walls of the bed while simultaneously expanding the entrainment region near the draft tube. This behavior is dynamic and visualized in Video S2 of the Supplementary Material, in which U_S is ramped up and down to demonstrate the evolution and suppression of gas bubbles in the annular region.

The extent of the gas leakage from the annular region is a result of the operational and geometric parameters of the DTSFB (U_S, U_{bg} and H_g), and further depends on the size of the inlet nozzle, the angle of the bottom plate, the draft tube diameter, and the particle size [12]. Depending on the exact settings of the operational and geometric parameters, more complex gas flow fields can establish, e.g., for large values of H_g, the venturi effect into the draft tube diminishes such that the spouting gas can escape from the draft tube and flow into the annular region leading to a reversed direction of the net gas leakage from the annular region. Even mutual leakage of gas from the annular region into the draft tube and vice versa is possible [16,18,19,67]. In the present study, the gap heights are small, with very little gas leakage from the spouting gas into the annular region, hence, gas leakage is directed from the annular region to the draft tube exclusively.

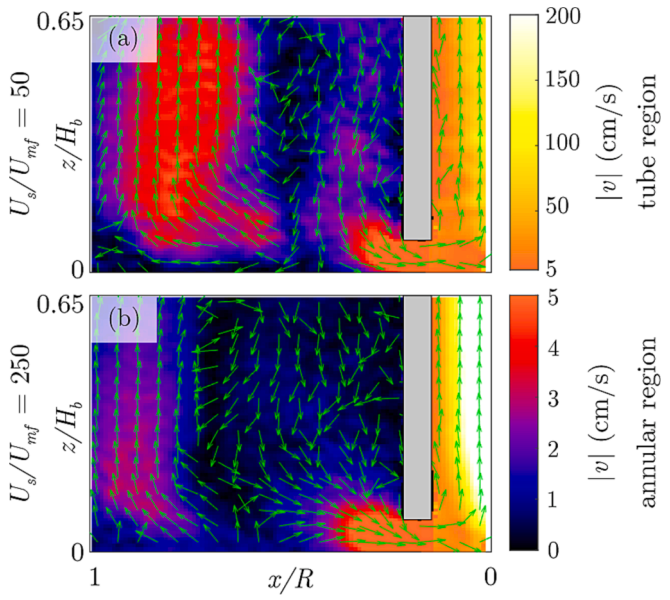

FIG.7. Particle velocity map in the annular region for $U_S/U_{mf} = 50$ (a) and 250 (b) with $H_g = 10$ mm and $U_{bg}/U_{mf} = 1.2$. The velocity map is obtained by averaging the left and the right side of the annular region.

3.4. Horizontal slices and radial distribution of particle velocity

In the following, the flow profile of particles in horizontal slices of the DTSFB is analyzed and illustrated in Fig. 8. To this end, three horizontal slices of thickness 10 mm were acquired at different heights (z = 5 mm, 15 mm, 25 mm) over the bottom section of the annular region in which we expect an entrainment zone. The position of these planes is visualized in Fig. 8 (a). Fig. 8 (b) and (c) quantify the radial (v_r) and vertical component (v_z) of the solid velocity, respectively. The insets in both figures show the velocity map in the annular region of the yellow slice at $z = 5$ mm, i.e., the vertical position of the slice coincides with the lower end of the draft tube. Both insets reveal the existence of a pronounced entrainment zone that is characterized by a negative vertical velocity (i.e., downwards, blue) and negative radial velocity (i.e., inwards, blue) near the draft tube. The boundary of the entrainment zone can be identified as the locus of zero radial or vertical velocity. For both velocity components the entrainment zone is fairly circular. Due to this circularity, the v_r and v_z data was averaged azimuthally to obtain the radial profiles $v_r(x, z)$ and $v_r(x, z)$ shown in the main panels of Fig. 8 (b) and (c). Inspecting such profiles in the annular region ($x/R > 0.15$), v_r and v_z decrease with increasing distance x from the draft tube until they reach a minimum velocity. Beyond this minimum, v_r and v_z increase again, cross the zero-velocity level and level off at low, positive velocities. Comparing the velocity profiles at the three heights $z = 5$ mm (yellow), 15 mm (orange) and 25 mm (blue) plotted in Fig. 8 (b) and (c), it can be seen that the minimum velocity increases with increasing height, z, of the measurement plane. Simultaneously, the position of this minimum and the position of zero velocity shift to larger radial distances from the draft tube, hence broadening the region of negative velocities. This indicates that the entrainment region grows with increasing height z but with decreasing entrainment speeds. The reciprocity between the entrainment speed and the size of the entrainment region agrees with the conservation of mass, assuming that the solid fraction is constant in the annular region.

In addition to the particle flow profile in the annular region, panels (b) and (c) also quantify the particle flow inside the draft tube ($x/R < 0.1$). Here, panel (b) shows that the radial direction of particle flow in the draft tube changes with the vertical position, i.e., it points inwards for $z = 5$ mm and outwards for $z = 15$ and 25 mm. This effect aligns with the observation of the vena contracta flow already observed in Fig. 3 (g) and Fig. 5 (a). The axial velocity profiles shown in Fig. 8 have been discussed at great depth in Section 3.2.

4. Conclusions

In this study, magnetic resonance imaging (MRI) velocimetry was used to non-invasively measure the hydrodynamics of the particle phase in a three-dimensional, draft tube spout-fluid bed (DTSFB) under various operational conditions at steady state. We observe the entrainment of particles from the annular region into the draft tube. Further, a previously unreported vena contracta structure was revealed at the bottom of the draft tube when operated at high spouting gas flows, indicating a particle transport limitation for small gap sizes. In addition, we observe a linear scaling of the vertical velocity of the particles in the draft tube with the velocity of the spouting gas, suggesting a dominant role of the spout on the particle motion in the draft tube. Importantly, there is also a strong effect of the velocity of the spouting gas on the fluidization behavior of the particles in the annular region. By increasing the velocity of the spouting gas, the area and intensity of bubbling fluidization in the annular region can be reduced significantly, indicating gas channeling from the annular region into the draft tube. The suppression of gas bubbling is most pronounced for DTSFBs with a low gap height, whereby gas bubbling can be even entirely absent in the annular region for a superficial background fluidization velocity higher than the minimum

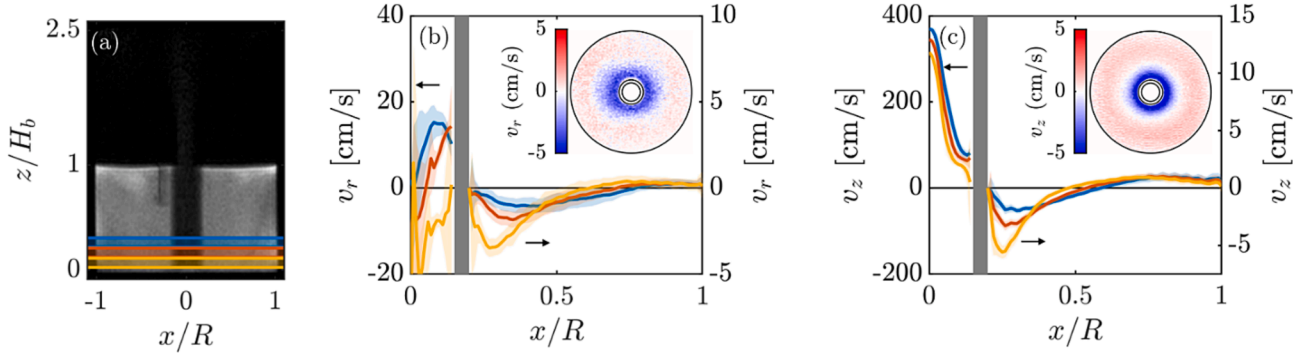

FIG.8. (a) Horizontal slices (10 mm thick) through the bottom section of the DTSFB at three heights z = 5 mm, 15 mm and 25 mm depicted by the yellow, orange, and blue slices, respectively. Radial particle velocity v_r (b) and vertical particle velocity v_z (c) in the three horizontal slices. The line plots show the azimuthally averaged radial profile of v_r and v_z in the annular region and the draft tube of the respective slice. The color of the slices in (a) corresponds to the line colors used in panel (b) and (c). The insets of (b) and (c) show the distribution of the respective velocity component in the horizontal slice at z = 5 mm (yellow slice). The walls of the draft tube are shown as grey limits. The standard deviation of the flow profiles is given as the shaded area. The standard deviation in panel (c) is very small. (For interpretation of the references to color in this figure legend, the reader is referred to the web version of this article.)

fluidization velocity. Numerical simulations confirm gas channeling from the annular region to the draft tube due to a pressure gradient between these two zones.

CRediT authorship contribution statement

Jens P. Metzger: Conceptualization, Data curation, Formal analysis, Investigation, Methodology, Software, Validation, Visualization, Writing – original draft, Writing – review & editing, Project administration. **Boyuan Chen:** Conceptualization, Data curation, Formal analysis, Investigation, Methodology, Software, Validation, Visualization, Writing – original draft, Writing – review & editing. **Alexander Penn:** Methodology, Resources, Validation, Writing – review & editing, Supervision. **Christian Guenthner:** Methodology, Resources, Supervision, Validation, Writing – review & editing. **Klaas P. Pruessmann:** Resources, Supervision, Writing – review & editing, Methodology, Validation. **Christoph R. Müller:** Conceptualization, Funding acquisition, Methodology, Project administration, Resources, Supervision, Validation, Writing – review & editing.

Declaration of competing interest

The authors declare that they have no known competing financial interests or personal relationships that could have appeared to influence the work reported in this paper.

Data availability

All relevant data supporting the findings of this study are either included within the article, its Supplementary Material files and in the Data Repository [56] or available upon request from the corresponding author.

Acknowledgements

This work was supported by the Swiss National Science Foundation (grant number 200020_ 182692) and was created as part of NCCR Catalysis (grant number 180544), a National Center of Competence in Research funded by the Swiss National Science Foundation.

Appendix A. Supplementary data

Supplementary data to this article can be found online at https://doi.org/10.1016/j.cej.2024.149678.

References

[1] N. Epstein, J.R. Grace, Introduction, in: J.R. Grace, N. Epstein (Eds.), Spouted and Spout-Fluid Beds: Fundamentals and Applications, Cambridge University Press, Cambridge, 2010, pp. 1–16, 10.1017/CBO9780511777936.002.
[2] W. Zhong, B. Jin, M. Zhang, R. Xiao, Hydrodynamics of spout-fluid beds, in: J. R. Grace, N. Epstein (Eds.), Spouted and Spout-Fluid Beds: Fundamentals and Applications, Cambridge University Press, Cambridge, 2010, pp. 105–127, https://doi.org/10.1017/CBO9780511777936.007.
[3] Y.J. Shao, X.J. Liu, W.Q. Zhong, B.S. Jin, M.Y. Zhang, Recent advances of spout-fluid bed: A review of fundamentals and applications, Int. J. Chem. React. Eng. 11 (2013) 243–258, https://doi.org/10.1515/ijcre-2013-0065.
[4] Z. Liu, H. Wang, S. Sun, L. Xu, W. Yang, Investigation of wetting and drying process in a spout-fluid bed using acoustic sensor and electrical capacitance tomography, Chem. Eng. Sci. 281 (2023) 119160, https://doi.org/10.1016/j.ces.2023.119160.
[5] S. Heinrich, M. Dosta, S. Antonyuk, Chapter two - multiscale analysis of a coating process in a wurster fluidized bed apparatus, in: G.B. Marin, J. Li (Eds.), Advances in Chemical Engineering, Academic Press, 2015, pp. 83–135, https://doi.org/10.1016/bs.ache.2015.10.012.
[6] J.L. Plawsky, H. Littman, J.D. Paccione, Design, simulation, and performance of a draft tube spout fluid bed coating system for aerogel particles, Powder Technol. 199 (2) (2010) 131–138, https://doi.org/10.1016/j.powtec.2009.12.009.
[7] J. Zhao, C.J. Lim, J.R. Grace, Flow regimes and combustion behaviour in coal-burning spouted and spout-fluid beds, Chem. Eng. Sci. 42 (12) (1987) 2865–2875, https://doi.org/10.1016/0009-2509(87)87052-5.
[8] M.S.T.J. Arnold, J.J. Gale, M.K. Laughlin, The british coal spouted fluidised bed gasification process, Can. J. Chem. Eng. 70 (5) (1992) 991–997, https://doi.org/10.1002/cjce.5450700522.
[9] J.L. Plawsky, S. Jovanovic, H. Littman, K.C. Hover, S. Gerolimatos, K. Douglas, Exploring the effect of dry premixing of sand and cement on the mechanical properties of mortar, Cement Concrete Res. 33 (2) (2003) 255–264, https://doi.org/10.1016/S0008-8846(02)00927-4.
[10] Z.B. Grbavcic, D.V. Vukovic, S.D. Jovanovic, R.V. Garic, D.E. Hadzismajlovic, H. Littman, M.H. Morgan, Fluid-flow pattern and solids circulation rate in a liquid-phase spout fluid bed with draft tube, Can. J. Chem. Eng. 70 (5) (1992) 895–904, https://doi.org/10.1002/cjce.5450700510.
[11] J. Xu, J.L. Tang, W.S. Wei, X.J. Bao, Minimum spouting velocity in a spout-fluid bed with a draft tube, Can. J. Chem. Eng. 87 (2) (2009) 274–278, https://doi.org/10.1002/cjce.20145.
[12] Ž.B. Grbavčić, H. Littman, M.H. Morgan, J.D. Paccione, Spouted and spout-fluid beds with draft tubes, in: J.R. Grace, N. Epstein (Eds.), Spouted and Spout-Fluid Beds: Fundamentals and Applications, Cambridge University Press, Cambridge, 2010, pp. 128–140, https://doi.org/10.1017/CBO9780511777936.008.
[13] F. Berruti, J.R. Muir, L.A. Behie, Solids circulation in a spout fluid bed with draft tube, Can. J. Chem. Eng. 66 (6) (1988) 919–923, https://doi.org/10.1002/cjce.5450660604.
[14] J.R. Muir, F. Berruti, L.A. Behie, Solids circulation in spouted and spout-fluid beds with draft-tubes, Chem. Eng. Commun. 88 (1990) 153–171, https://doi.org/10.1080/00986449008940553.
[15] Y.M. Zhang, G.Q. Huang, G.L. Su, Hydrodynamic behavior of silicon particles with a wide size distribution in a draft tube spout-fluid bed, Chem. Eng. J. 328 (2017) 645–653, https://doi.org/10.1016/j.cej.2017.07.071.
[16] R. Xiao, M.Y. Zhang, B.S. Jin, X.D. Liu, Solids circulation flux and gas bypassing in a pressurized spout-fluid bed with a draft tube, Can. J. Chem. Eng. 80 (5) (2002) 800–808, https://doi.org/10.1002/cjce.5450800503.
[17] H. Nagashima, T. Ishikura, M. Ide, Flow regimes and vertical solids conveying in a spout-fluid bed with a draft tube, Can. J. Chem. Eng. 89 (2) (2011) 264–273, https://doi.org/10.1002/cjce.20403.
[18] A. Çeçen Erbıl, Annulus leakage and distribution of the fluid flow in a liquid spout–fluid bed with a draft tube, Chem. Eng. Sci. 58 (20) (2003) 4739–4745, https://doi.org/10.1016/j.ces.2003.05.005.
[19] A.C. Erbil, Effect of the annulus aeration on annulus leakage and particle circulation in a three-phase spout-fluid bed with a draft tube, Powder Technol. 162 (1) (2006) 38–49, https://doi.org/10.1016/j.powtec.2005.11.006.
[20] M.C. Matthew, M.H. Morgan, H. Littman, Study of the hydrodynamics within a draft tube spouted bed system, Can. J. Chem. Eng. 66 (6) (1988) 908–918, https://doi.org/10.1002/cjce.5450660603.
[21] H. Nagashima, Y. Kawashiri, K. Suzukawa, T. Ishikura, Effects of operating parameters on hydrodynamic behavior of spout-fluid beds without and with a draft tube, Procedia, Engineer 102 (2015) 952–958, https://doi.org/10.1016/j.proeng.2015.01.217.
[22] V.S. Sutkar, N.G. Deen, V. Salikov, S. Antonyuk, S. Heinrich, J.A.M. Kuipers, Experimental and numerical investigations of a pseudo-2d spout fluidized bed with draft plates, Powder Technol. 270 (2015) 537–547, https://doi.org/10.1016/j.powtec.2013.11.030.
[23] V.S. Sutkar, T.J.K. van Hunsel, N.G. Deen, V. Salikov, S. Antonyuk, S. Heinrich, J.A. M. Kuipers, Experimental investigations of a pseudo-2d spout fluidized bed with draft plates, Chem. Eng. Sci. 102 (2013) 524–543, https://doi.org/10.1016/j.ces.2013.08.046.
[24] S.J. Kim, Fluid and particle flow characteristics in a draft tube spouted bed with modified fluid outlet, Korean J. Chem. Eng. 7 (1) (1990) 74–80, https://doi.org/10.1007/Bf02697345.
[25] B.A. Saadevandi, R. Turton, Particle velocity and voidage profiles in a draft tube equipped spouted-fluidized bed coating device, Chem. Eng. Commun. 191 (10) (2004) 1379–1400, https://doi.org/10.1080/00986440490472661.
[26] M. Knezevic, D. Povrenovic, Influence of fluid-mechanical parameters on volumetric mass transfer coefficient in a spout-fluid bed with a draft tube, Chem. Eng. Sci. 134 (2015) 129–137, https://doi.org/10.1016/j.ces.2015.04.030.
[27] J.Y. Day, M.H. Morgan, H. Littman, Measurements of spout voidage distributions, particle velocities and particle circulation rates in spouted beds of coarse particles—ii. Experimental verification, Chem. Eng. Sci. 42 (6) (1987) 1461–1470, https://doi.org/10.1016/0009-2509(87)85018-2.
[28] A. Benkrid, H.S. Caram, Solid flow in the annular region of a spouted bed, AIChE J. 35 (8) (1989) 1328–1336, https://doi.org/10.1002/aic.690350811.
[29] Y.-L. He, S.-Z. Qin, C.J. Lim, J.R. Grace, Particle velocity profiles and solid flow patterns in spouted beds, Can. J. Chem. Eng. 72 (4) (1994) 561–568, https://doi.org/10.1002/cjce.5450720402.
[30] Y.-L. He, C.J. Lim, J.R. Grace, J.-X. Zhu, S.-Z. Qzn, Measurements of voidage profiles in spouted beds, Can. J. Chem. Eng. 72 (2) (1994) 229–234, https://doi.org/10.1002/cjce.5450720208.
[31] M. Olazar, M.a.J. San José, M.A. Izquierdo, A.O. de Salazar, J. Bilbao, Effect of operating conditions on solid velocity in the spout, annulus and fountain of spouted beds, Chem. Eng. Sci. 56 (11) (2001) 3585–3594, https://doi.org/10.1016/S0009-2509(01)00022-7.
[32] J.M. Link, W. Godlieb, P. Tripp, N.G. Deen, S. Heinrich, J.A.M. Kuipers, M. Schönherr, M. Peglow, Comparison of fibre optical measurements and discrete element simulations for the study of granulation in a spout fluidized bed, Powder Technol. 189 (2) (2009) 202–217, https://doi.org/10.1016/j.powtec.2008.04.017.
[33] B. Wu, A. Orta, A. Kantzas, Experimental flow measurements of a spouted bed using pressure transducer and x-ray ct scanner, Int. J. Chem. React. Eng. 9 (1) (2011), https://doi.org/10.1515/1542-6580.2522.

[34] X. Yang, J.R. van Ommen, E. Wagner, R.F. Mudde, Time-resolved characterization of a flat-base spouted bed with a high speed x-ray system, Chem. Eng. J. 254 (2014) 143–152, https://doi.org/10.1016/j.cej.2014.05.050.
[35] M. Bieberle, F. Barthel, Combined phase distribution and particle velocity measurement in spout fluidized beds by ultrafast x-ray computed tomography, Chem. Eng. J. 285 (2016) 218–227, https://doi.org/10.1016/j.cej.2015.10.003.
[36] M. Al-Shemmeri, K. Windows-Yule, E. Lopez-Quiroga, P.J. Fryer, Coffee bean particle motion in a spouted bed measured using positron emission particle tracking (pept), J. Food. Eng. 311 (2021), https://doi.org/10.1016/j.jfoodeng.2021.110709.
[37] H.Q. Che, M. Al-Shemmeri, P.J. Fryer, E. Lopez-Quiroga, T.K. Wheldon, K. Windows-Yule, Pept validated cfd-dem model of aspherical particle motion in a spouted bed, Chem. Eng. J. 453 (2023), https://doi.org/10.1016/j.cej.2022.139689.
[38] J.M. Link, N.G. Deen, J.A.M. Kuipers, X. Fan, A. Ingram, D.J. Parker, J. Wood, J.P. K. Seville, Pept and discrete particle simulation study of spout-fluid bed regimes, AIChE J. 54 (5) (2008) 1189–1202, https://doi.org/10.1002/aic.11456.
[39] C. Seiler, P.J. Fryer, J.P.K. Seville, Statistical modelling of the spouted bed coating process using positron emission particle tracking (pept) data, Can. J. Chem. Eng. 86 (3) (2008) 571–581, https://doi.org/10.1002/cjce.20053.
[40] G. Mohs, O. Gryczka, S. Heinrich, L. Mörl, Magnetic monitoring of a single particle in a prismatic spouted bed, Chem. Eng. Sci. 64 (23) (2009) 4811–4825, https://doi.org/10.1016/j.ces.2009.08.025.
[41] E.E. Patterson, J. Halow, S. Daw, Innovative method using magnetic particle tracking to measure solids circulation in a spouted fluidized bed, Ind. Eng. Chem. Res. 49 (11) (2010) 5037–5043, https://doi.org/10.1021/ie9008698.
[42] M.S. van Buijtenen, K. Buist, N.G. Deen, J.A.M. Kuipers, T. Leadbeater, D.J. Parker, Numerical and experimental study on spout elevation in spout-fluidized beds, AIChE J. 58 (8) (2012) 2524–2535, https://doi.org/10.1002/aic.12765.
[43] T. Kawaguchi, T. Yoshida, Y. Tsuji, Mri measurement of particle velocity in spouted bed, J. Japan. Soc, Exp. Mech. 7 (Special_Issue) (2007) s12–s16, https://doi.org/10.11395/jjsem.7.s12.
[44] C.R. Muller, D.J. Holland, A.J. Sederman, J.S. Dennis, L.F. Gladden, Magnetic resonance measurements of high-velocity particle motion in a three-dimensional gas-solid spouted bed, Phys. Rev. E 82 (5) (2010), https://doi.org/10.1103/PhysRevE.82.050302.
[45] M.H. Köhl, G. Lu, J.R. Third, K.P. Pruessmann, C.R. Müller, Magnetic resonance imaging (mri) of jet height hysteresis in packed beds, Chem. Eng. Sci. 109 (2014) 276–283, https://doi.org/10.1016/j.ces.2014.01.038.
[46] A. Penn, C.M. Boyce, K.P. Pruessmann, C.R. Müller, Regimes of jetting and bubbling in a fluidized bed studied using real-time magnetic resonance imaging, Chem. Eng. J. 383 (2020) 123185, https://doi.org/10.1016/j.cej.2019.123185.
[47] V.S. Sutkar, N.G. Deen, B. Mohan, V. Salikov, S. Antonyuk, S. Heinrich, J.A. M. Kuipers, Numerical investigations of a pseudo-2d spout fluidized bed with draft plates using a scaled discrete particle model, Chem. Eng. Sci. 104 (2013) 790–807, https://doi.org/10.1016/j.ces.2013.10.005.
[48] S.H. Hosseini, M. Zivdar, R. Rahimi, Cfd simulation of gas-solid flow in a spouted bed with a non-porous draft tube, Chem. Eng. Process. 48 (11–12) (2009) 1539–1548, https://doi.org/10.1016/j.cep.2009.09.004.
[49] M.R. Rahimi, S. Azizi, Cfd multifluid simulation of spouted beds with and without internal draft tubes, Chem. Prod. Process Mo. 6 (1) (2011), https://doi.org/10.2202/1934-2659.1559.
[50] S.Y. Wang, Z.H. Hao, D. Sun, Y.K. Liu, L.X. Wei, S.A. Wang, Hydrodynamic simulations of gas-solid spouted bed with a draft tube, Chem. Eng. Sci. 65 (4) (2010) 1322–1333, https://doi.org/10.1016/j.ces.2009.09.060.
[51] S.L. Yang, K. Luo, M.M. Fang, J.R. Fan, Discrete element simulation of the hydrodynamics in a 3d spouted bed: Influence of tube configuration, Powder Technol. 243 (2013) 85–95, https://doi.org/10.1016/j.powtec.2013.03.041.
[52] V.S. Sutkar, N.G. Deen, J.A.M. Kuipers, Spout fluidized beds: Recent advances in experimental and numerical studies, Chem. Eng. Sci. 86 (2013) 124–136, https://doi.org/10.1016/j.ces.2012.06.022.
[53] J.M. Link, L.A. Cuypers, N.G. Deen, J.A.M. Kuipers, Flow regimes in a spout-fluid bed: A combined experimental and simulation study, Chem. Eng. Sci. 60 (13) (2005) 3425–3442, https://doi.org/10.1016/j.ces.2005.01.027.
[54] J.N. Zhao, G.D. Liu, X.L. Yin, X.H. Li, Z.Y. Gao, H.L. Lu, Two-fluid simulation of a three-dimensional spout-fluid bed: Flow structures, regimes, and insight into the mechanism of particle-particle momentum transfer, Ind. Eng. Chem. Res. 60 (21) (2021) 7950–7965, https://doi.org/10.1021/acs.iecr.1c00928.
[55] C. Goniva, C. Kloss, N.G. Deen, J.A.M. Kuipers, S. Pirker, Influence of rolling friction on single spout fluidized bed simulation, Particuology 10 (5) (2012) 582–591, https://doi.org/10.1016/j.partic.2012.05.002.
[56] J.P. Metzger, B. Chen, A. Penn, C. Guenthner, K.P. Pruessmann, C.R. Müller, Magnetic resonance velocimetry of particle hydrodynamics in a three-dimensional draft tube spout-fluid bed, (data) (2023), https://doi.org/10.5281/zenodo.10677372.
[57] A. Penn, T. Tsuji, D.O. Brunner, C.M. Boyce, K.P. Pruessmann, C.R. Müller, Real-time probing of granular dynamics with magnetic resonance, Sci. Adv. 3 (9) (2017) e1701879.
[58] D. Geldart, Types of gas fluidization, Powder Technol. 7 (5) (1973) 285–292, https://doi.org/10.1016/0032-5910(73)80037-3.
[59] F.R. Menter, Two-equation eddy-viscosity turbulence models for engineering applications, AIAA J. 32 (8) (1994) 1598–1605, https://doi.org/10.2514/3.12149.
[60] R.J. Hill, D.L. Koch, A.J.C. Ladd, Moderate-reynolds-number flows in ordered and random arrays of spheres, J. Fluid Mech. 448 (2001) 243–278, https://doi.org/10.1017/S0022112001005936.
[61] H. Dillinger, C. McGrath, C. Guenthner, S. Kozerke, Fundamentals of turbulent flow spectrum imaging, Magn. Reson. Med. 87 (3) (2022) 1231–1249, https://doi.org/10.1002/mrm.29001.
[62] M. Mehdizad, L. Fullard, P. Galvosas, D. Holland, Quantitative measurements of flow dynamics in 3d hoppers using mri, Powder Technol. 392 (2021) 69–80, https://doi.org/10.1016/j.powtec.2021.06.048.
[63] M. Mehdizad, L. Fullard, P. Galvosas, D. Holland, Quantitative measurement of solid fraction in a silo using sprite, J. Magn. Reson. 325 (2021) 106935, https://doi.org/10.1016/j.jmr.2021.106935.
[64] N. Epstein, J.R. Grace, Spouting of particulate solids, in: M.E. Fayed, L. Otten (Eds.), Handbook of powder science & technology, Springer US, Boston, MA, 1997, pp. 532-567. https://doi.org/10.1007/978-1-4615-6373-0_10.
[65] W. Zhang, Y. Tung, F. Johnsson, Radial voidage profiles in fast fluidized-beds of different diameters, Chem. Eng. Sci. 46 (12) (1991) 3045–3052, https://doi.org/10.1016/0009-2509(91)85008-L.
[66] H. Zhang, W.X. Huang, J.X. Zhu, Gas-solids flow behavior: Cfb riser vs, Downer, AIChE J. 47 (9) (2001) 2000–2011, https://doi.org/10.1002/aic.690470911.
[67] W.C. Yang, D.L. Keairns, Studies on the solid circulation rate and gas bypassing in spouted fluid-bed with a draft tube, Can. J. Chem. Eng. 61 (3) (1983) 349–355, https://doi.org/10.1002/cjce.5450610314.